Plant Scaffolds Support Motor Recovery and Regeneration in Rat Spinal Cord Injury

Daniel J. Modulevsky[1,2], Charles M. Cuerrier[1,2,3], Maxime Leblanc-Latour[1,3], Ryan J. Hickey[1], Ras-Jeevan K. Obhi[1], Isabel Shore[1,3], Ahmad Galuta[4], Krystal L. A. Walker[4], Eve C. Tsai[4,5,6] and Andrew E. Pelling[1,2,3,7,8*]

[1]*Department of Physics, STEM Complex, 150 Louis Pasteur Pvt., University of Ottawa, Ottawa, ON, K1N5N5 Canada*

[2]*Department of Biology, Gendron Hall, 30 Marie Curie, University of Ottawa, Ottawa, ON, K1N5N5 Canada*

[3]*Spiderwort Inc., 7, Bayview Station Road, Ottawa, ON, K1K4R3 Canada*

[4]*Program in Neuroscience, Ottawa Hospital Research Institute, Ottawa, ON, K1Y 4E9 Canada*

[5]*Division of Neurosurgery, Department of Surgery, The Ottawa Hospital, Ottawa, ON, K1Y 4E9 Canada*

[6]*Department of Cellular and Molecular Medicine, Faculty of Medicine, University of Ottawa, Ottawa, ON, K1H 8M5 Canada*

[7]*Institute for Science Society and Policy, Simard Hall, 60 University, University of Ottawa, Ottawa, ON, K1N5N5 Canada*

[8]*SymbioticA, School of Human Sciences, University of Western Australia, Perth, WA, 6009 Australia*

*Author for correspondence: Andrew E. Pelling, University of Ottawa, Tel. +1 613 562 5800 Ext 6965, Fax. +1 613 562 5190, Email: a@pellinglab.net

Abstract

As of yet, no standard of care incorporates the use of a biomaterial to treat traumatic spinal cord injury (SCI)[1–5]. However, intense development of biomaterials for treating SCI have focused on the fabrication of microscale channels to support the regrowth of axons while minimizing scar tissue formation[6–10]. We previously demonstrated that plant tissues can be decellularized and processed to form sterile, biocompatible and implantable biomaterials that support cell infiltration and vascularization in vivo[11–13] Notably, the vascular bundles of plant tissues are also composed of microscale channels with geometries thought to be relevant for supporting neural tissue regeneration[14,15]. We hypothesized that decellularized vascular bundles would support neural regeneration and the recovery of motor function. Therefore, rats which received a completeT8-T9 spinal cord transection were implanted with plant-derived channeled scaffolds. Animals which received the scaffolds alone, with no therapeutic stem cells or other interventions, demonstrated a significant and stable improvement in motor function over six months compared to controls. Histological analysis reveals minimal scarring and axonal regrowth through the scaffolds, further confirmed with tracer studies. Taken together, our work defines a novel route for exploiting naturally occurring plant microarchitectures to support the repair of functional spinal cord tissue.

Introduction

The annual incidence of traumatic spinal cord injury (SCI) is as much as 51 per million people in developed countries, with mortality rates of 48-79%[16]. Although treating the devastating loss of motor function is the ultimate clinical goal, recovery of bowel, bladder, sexual and tactile function can all contribute to a significant improvement in patient quality of life[17]. While there are no accepted therapies to treat the underlying issue of scar and cyst

2

formation at the epicenter of the injury[1–5], one possible approach is the use of a biomaterial that promotes axonal regrowth, sequesters scar tissue and supports blood vessel formation, which can ultimately aid in the recovery of function[18]. There has been an intense effort to create scaffolds with 3D architectures designed to achieve this goal utilizing all manner of microfabrication techniques[6,7,9,10,19]. As such, the performance of many varieties of natural and synthetic polymers have been investigated in a number of SCI animal models[3,6,24–29,7–10,20–23]. In many studies, scaffolds demand supplementation with neural progenitor cells (NPCs), pharmaceuticals, or growth factors (alone or in combination) to achieve a desired effect[9,10] Oftentimes, tissue regeneration and improvement in motor recovery is only possible with combined strategies[9,30–34].

Results and Discussion

Previous work from our group, and others, has shown that microarchitecture in decellularized plant tissues are biocompatible in vitro[11–13,35–37] and in vivo[12,13,38]. Here, we investigated the stalks of *Asparagus officinalis* as a potential biomaterial as they contain linearly arranged, parallel microchannels which form vascular bundles (VBs) (Fig. 1a, b). The VBs are circularly arranged and separated from one another by parenchyma tissue with an average spacing of 612±70µm. The VBs are composed tissues which aid in the efficient transport of water, nutrients and biomolecules throughout the plant and their structures are preserved after decellularization (Fig. 1a, b). Scanning electron microscopy (SEM) of the VBs reveals a variety of tissue structures with characteristic diameters, such as xylem channels (51±15 µm), sieve tubes (40±16µm), parenchyma (35±8µm) and the phloem (9±2µm) (Fig. 1 c-e, Supplementary Fig. 1).

3

Due to the distribution of microchannels in their architecture, we hypothesized that decellularized vascular plant tissues could be exploited as lignocellulosic scaffolds for the repair of completely transected spinal cord in a rat model. On average, each scaffold contained 11±2 VBs, each containing 35±5 microchannels. These channels were observed to be consistent in diameter and orientation throughout the entire scaffold and emerge in the same position on either end (Supplementary Fig. 2). Scaffolds were selected that contained the maximum number of VBs to promote invasion of regenerating axon projections in a completely transected spinal cord. The scaffolds are mechanically anisotropic due to the linear orientation of the VBs along the plant stem. This results in an elastic modulus of 148±53kPa (n=10) or 12±4 kPa (n=10) when measured parallel or perpendicular to the long axis, which is within the range of healthy rat spinal cords[39,40] (Supplementary Fig. 3).

In animals with a complete T8-T9 spinal cord transection, the scaffold group (n=18 animals), had grafts inserted with lengths to match the intra gap distance of the stumps. Fibrin was applied across the dorsal surface of the scaffold to fix it between the stumps (Fig 1f). The control group (n=13 animals) did not receive the scaffold and the fibrin was applied to the gap formed between the stumps. After 4 weeks, animals were imaged with the magnetic resonance imaging (MRI) to confirm that the scaffold remained in place (Fig. 1g, h). The rostral and caudal stumps of the transected spinal cord remain aligned with the scaffold, while in the control animals, typical symptoms of intermediate and chronic secondary spinal cord injuries were apparent[9,17,28,29,39–41].
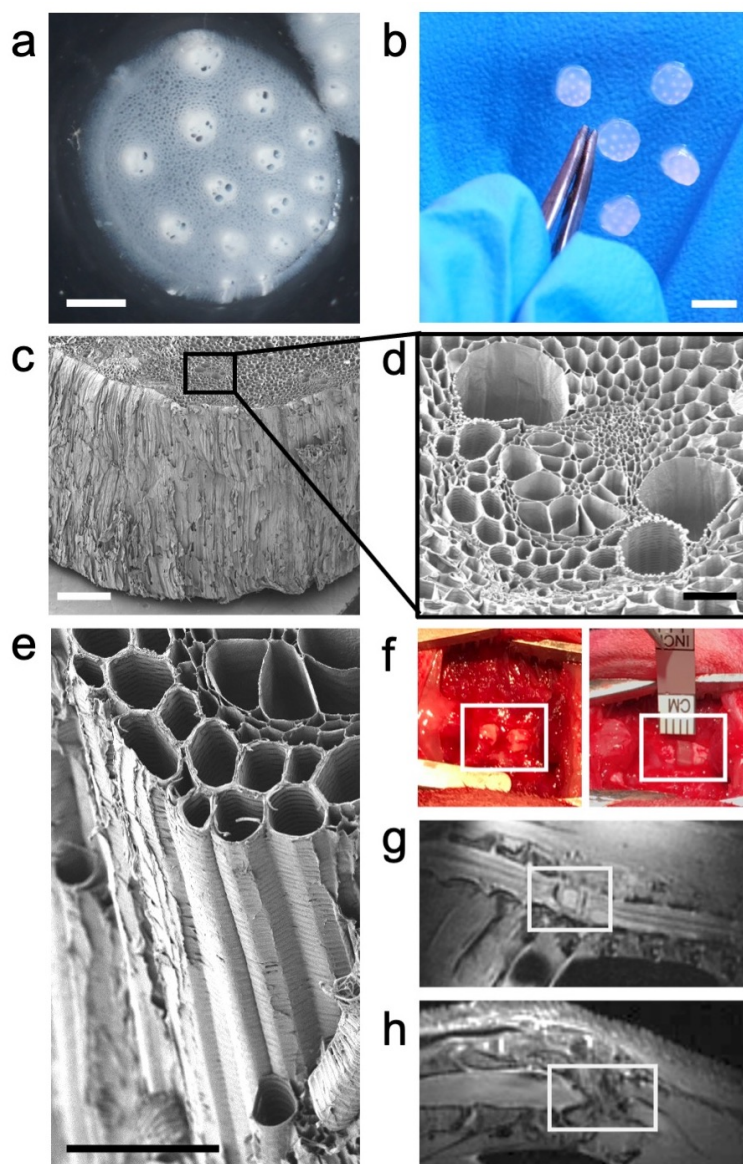
4

Fig. 1 | Plant-derived scaffolds for spinal cord injury.

a) Decellularized plant-derived scaffold with visible vascular bundles (VBs) surrounded by parenchyma (bar=1mm). **b)** VBs are even visible to the naked eye (bar=4mm). **c)** SEM reveals scaffolds also have a grooved outer topography (bar=300μm). **d)** Imaging the scaffold cross-section at higher magnification reveals a VB (bar=100μm). **e)** VB channel architecture runs the entire length of the scaffold (bar=100μm). **f)** An exposed fully transected spinal cord (left, box) and a scaffold after implantation (right, box). **g**) Sagittal MRI of T8-T9 injury (box) containing a scaffold after 4 weeks, and **h)** the resulting scar a control animal.

The motor recovery of the rats was blindly assessed using the established Basso, Beattie and Bresnahan (BBB) locomotor scale[42]. Rats that received the scaffold had a statistically significant (p=0.030655) functional recovery starting at week 4 (Fig 2a). Though both groups were observed to display some motor recovery, the degree of recovery was significantly higher in animals that received the scaffold. By week 4, control scores plateaued at 2.3±0.5 (extensive movement of one joint). Conversely, the scaffold group displayed continued improvement until week 7, after which the BBB score plateaued at 5.5±0.1 (extensive movement at all three hindlimb joints, p= 2.4×10^{-7}). This improvement in motor function was consistent with limb recovery and coordination that led to weight supported plantar stepping (Supplementary Fig. 4). The motor skills did not deteriorate significantly over the remainder of the 6 months (Fig. 2a). To rule out reflex adaptation, random animals were selected for an end point re-transection surgery at the T13 vertebra[43]. Animals were allowed to recover for one week before motor skill re-assessment. In the scaffold and control groups, motor recovery was lost and BBB scores of 0.3±0.2 and 0.1±0.1, respectively (p=0.251289794). The rats were euthanized and harvested at their respective end points of 14 and 28 weeks. Tissue was sectioned in either an axial or sagittal orientation (Fig. 2b-f) and stained with hematoxylin and eosin (H&E). It was observed during the dissection that the scaffold was well integrated well enough between the two stumps of the spinal cord that the entire structure could be moved as one unit. The control groups were difficult to remove as the stumps were loosely adhered via scar and connective tissues. These observations are consistent with MRI which revealed that the scaffold formed a physical bridge between the spinal cord stumps (Fig. 1g)

At 14 weeks, H&E staining revealed that the scaffold retained its pre-implant size. Although macrophages were present, there was no observable degradation of the scaffold (Fig.

6

2b). The VBs within the scaffold were infiltrated with cells throughout its length between the spinal cord stumps (Fig. 2c, d). Almost no foreign multinucleated cells, basophils cells or lymphocytes associated with chronic foreign body response (FBR), were observed (Fig. 2e). Importantly, at 28 weeks H&E imaging revealed results highly consistent with the 14 week time point (Supplementary Fig. 5). Moreover, the control animal injury site was void of cell infiltration, with cysts forming at the site of transection, as is typical with untreated SCI transection injuries[3] (Fig. 2f). Capillaries and blood vessels were found in 86% of all VBs, which demonstrated that the channels of the scaffold support vascularization throughout the injury site (Fig. 2e), consistent with our previous in vivo studies[12,13]. The vascularized VBs are then likely able to supply infiltrating cells in the nearby scaffold tissues with nutrients/oxygen. This is consistent with the observation of host fibroblast cells migrate within the interstitial spaces formed by the overlapping plant cell walls in the parenchyma tissue (Fig. 2d, e). The largest channels of VBs were observed to incorporate the majority of granulation scar tissue or mature blood vessels characterized by a thick endothelial lining (Fig. 2e). Thus, the mammalian scar tissue response appeared to be largely sequestered to the VB elements (Supplementary Fig. 6).
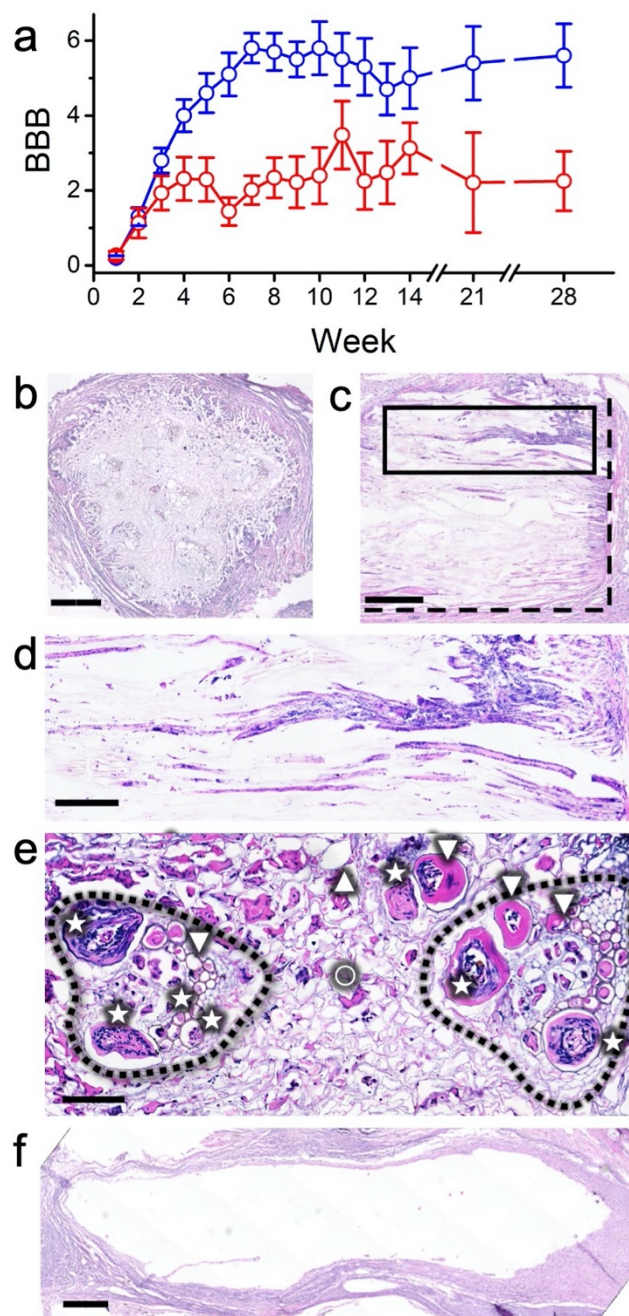
Fig 2. | Motor recovery and histology after 14 weeks post injury.
a) BBB motor scores after complete transection in animals with (blue) and without (red) a scaffold are significantly different from week 4 (p=0.030655) and onwards. **b)** Axial H&E of scaffold. VBs are infiltrated with host cells (bar=400μm). **c)** Sagittal H&E of the scaffold (bar =500μm) and **d)** higher magnification of the boxed (bar=250μm). VBs are infiltrated from the stumps and cells are observed throughout the scaffold (scaffold-tissue interface (dotted line)). **e)** H&E of two VBs (dotted lines) after 14 weeks. Blood vessels (∇), granulation tissue ($\bigstar$) are observed in the VBs. The parenchyma (o) between the VBs contains fibroblasts ($\triangle$) (bar=100 μm) **f)** Sagittal H&E of a control animal spinal cord for comparison (bar=500μm).

The formation of astrocyte scarring was assessed by glial fibrillary acidic protein (GFAP) labelling. The rostral and caudal ends of the scaffold-spinal cord interface both displayed low GFAP scarring when compared to the control animal stump (Fig. 3a-c). The thickness of the GFAP labelled astrocyte scarring when present around the biomaterial was measured at 54 ± 3.5 μm, significantly less than the control animals at $159 \pm 8 \mu m$ ($p=1.23631 \times 10^{-17}$) (Fig. 3d). These results were consistent with the inhibition of astrocyte scarring in previously reported synthetic cellulose-based scaffolds[6]. When GFAP-positive astrocytes were observed in the scaffold and surrounding tissue they were generally located within the largest diameter VBs. Though the precise role of glial scar tissue is still not known, scarring was observed to be segregated within the large diameter channels[43–45]. This left the parenchymal tissue and smaller VBs available for projecting axons.

Host axons, labelled with neurofilament protein NF200 were observed regenerating readily throughout the entire scaffold in a linear orientation along the median axis of the spinal cord (Fig. 3e-g). Axon density in the scaffolds (545 ± 37 axons/mm^2) was significantly higher ($p=0.01859$) than in the tissue of the control scar tissue (368 ± 62 axons/mm^2) (Fig. 3h). Cells and axons surrounding the scaffold were also observed to be aligned to external linear topography (Fig. 1e, Fig. 3i) of the biomaterial, consistent with contact guidance[46]. Minimal scar tissue was also observed in these regions (Fig. 3j). These results suggest that the scaffold provides a microenvironment that promotes the growth of native axons while inhibiting uncontrolled astrogliosis.
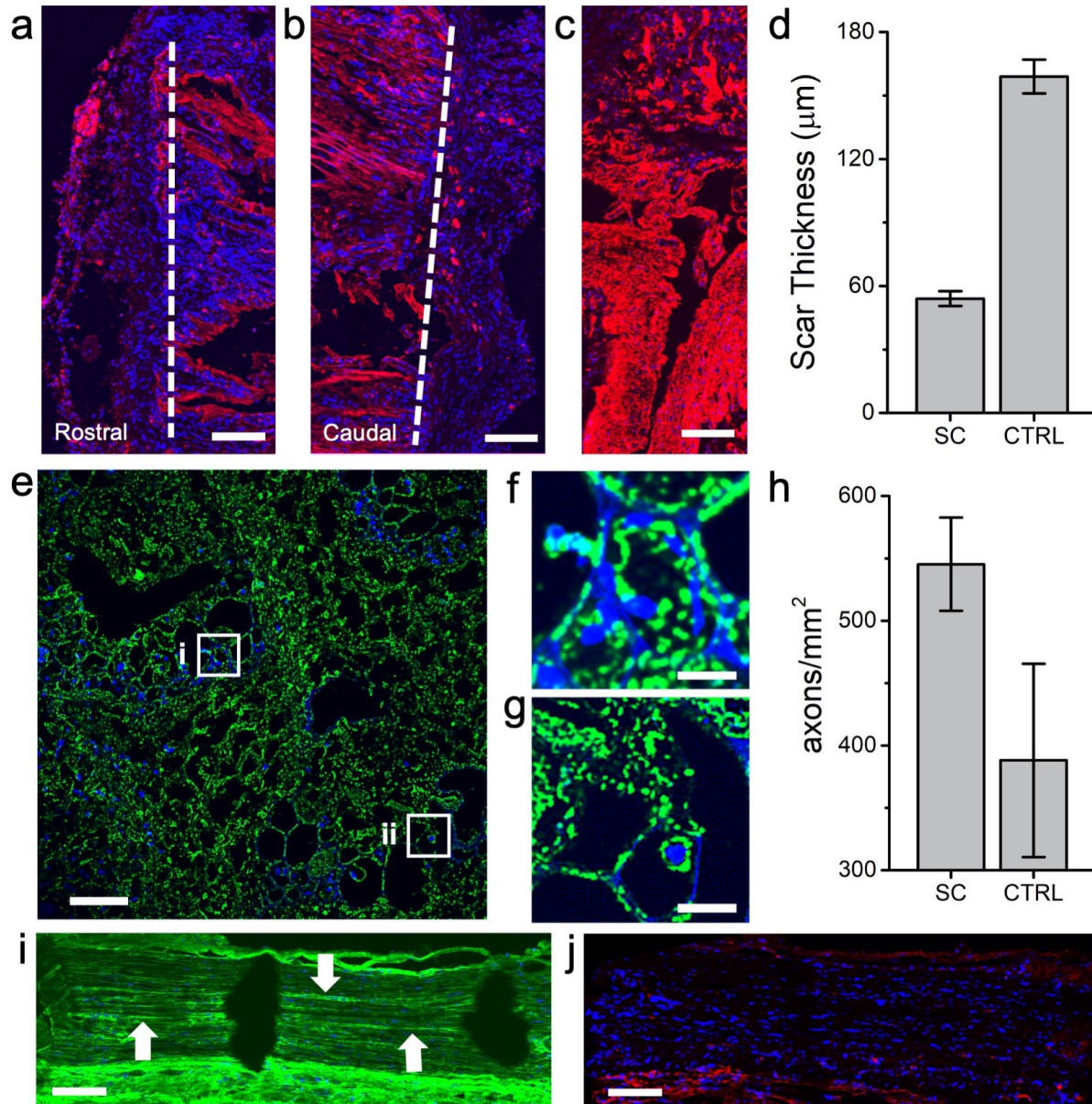
9

Fig 3. NF200 and GFAP staining 14 weeks post injury. a) Rostral end, sagittal view of the scaffold interface (dotted line) with spinal cord stained for GFAP (red) and DAPI (blue) (bar=500µm, for a to c). **b)** Caudal end, Sagittal view of the same implant. **c)** Axial section of GFAP and DAPI stained control animals. **d)** The thickness of the GFAP astrocyte scar tissue in scaffolds (SC) vs control (CTRL) (p=1.23631x10^{-17}). **e)** Axial section within the scaffold of NF200 (green) and DAPI (blue) after 14 weeks (bar=100µm). Magnification of the boxed areas **i** and **ii** are shown in **f)** and **g)**, respectively (bar=25µm). **h)** The density NF200 labelled axons within the scaffold and control tissue (p=0.01859). **i)** Sagittal view of longitudinal of the tissues on the dorsal surface of the scaffold. Axons appear in a linear orientation (arrows) (bar=125µm). **j)** Another sagittal view reveals limited scarring in tissues on the dorsal surface of the scaffold (bar=125µm).

To determine the functionality of axons projecting into the scaffold from the rostral and caudal ends, we utilized retrograde axonal tracing with Fluorogold (FG)[47]. Animals that underwent a secondary complete transection at T13 (Fig. 4a), had the FG applied to the rostral aspect of the cut cord that retrogradely labeled the cell bodies of neurons. FG labelled axons were observed inside the scaffold on both the rostral and caudal ends (Fig. 4b, c). An axial section of the scaffold also revealed the presence of point-like structures consistent with axon morphology (Fig. 4d) and NF200 staining (Fig. 3e-g). Importantly, FG positive cell bodies and axons were observed in the rostral spinal cord tissue across the scaffold (Fig. 4e). In control experiments, we observed low FG signal, and a lack of non-specific FG wicking through the scaffold in negative controls (Supplementary Fig. 8). These results confirmed that FG-positive cells were a result of retrograde axonal transport. FG intensity and FG positive cell counts were quantified in the spinal cord rostral and caudal to the scaffold (Fig. 4f). The number of FG-positive cells on the rostral side of the injury was significantly decreased compared to the caudal end in control animals (p=0.01102), which was not the case in animals that received a scaffold (p=0.77785). Likewise, FG intensity nearly disappeared across the transection in the control animals (p=0.00278). Conversely, in animals that received a scaffold, FG intensity remained constant (p=0.59004). The results demonstrate the presence of axonal connections between neurons on the caudal side of the scaffold to axons and cell bodies on the rostral side (Supplementary Fig. 9).
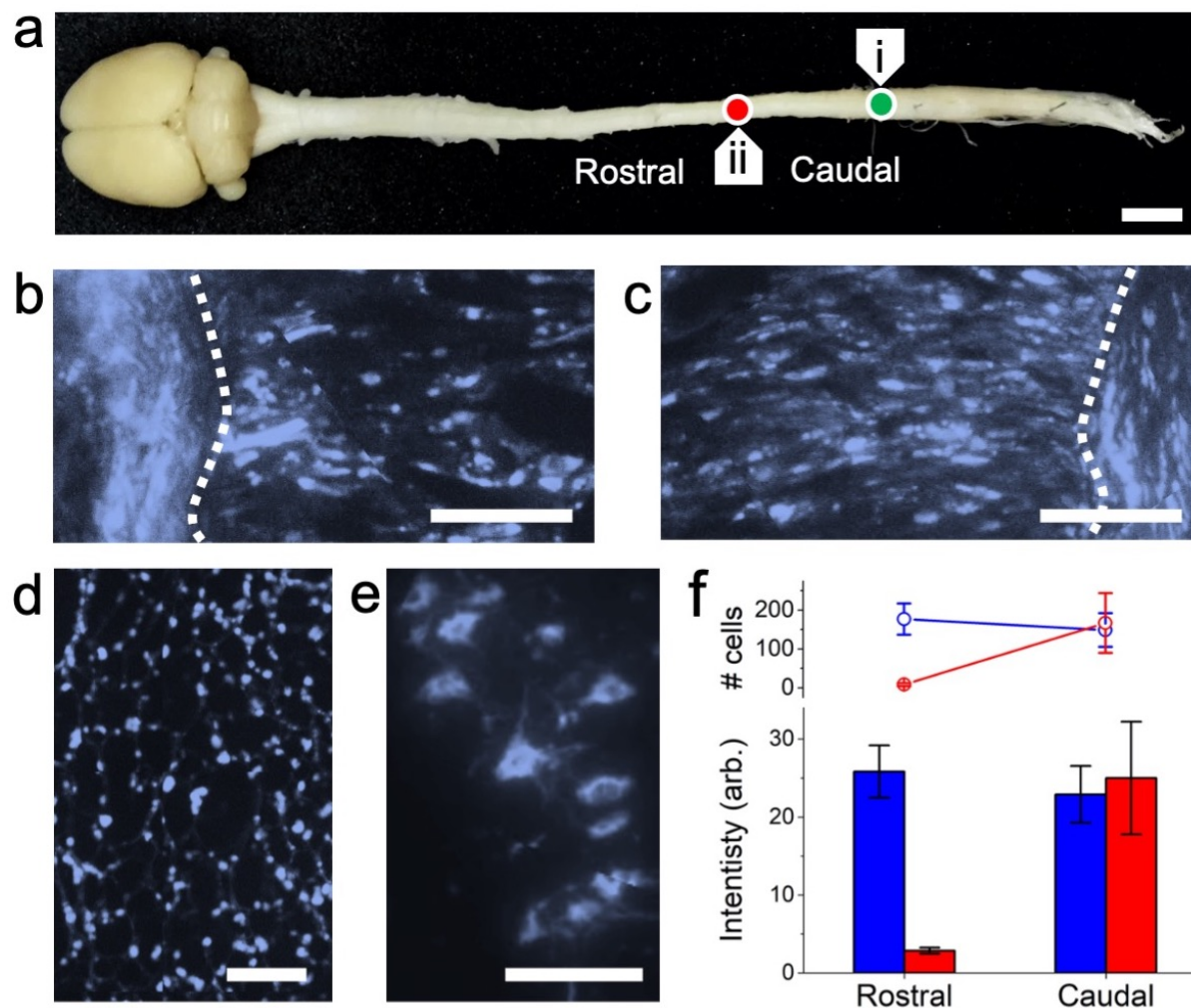
Fig 4. Retrograde axonal tracing weeks post injury. a) Some animals received a secondary transection (i) at T13 caudal to the original injury (ii) and FG was loaded into the new site (healthy CNS shown for illustration). One week later, sagittal sections of the **b)** rostral and **c)** caudal ends of the scaffold reveal projecting axons at the scaffold-tissue interface (dotted line) (bar=100μm). **d)** Axial section of the scaffold with FG positive axons (bar=100μm). **e)** A magnified view of the rostral spinal cord with FG positive cell bodies and axons (bar=100μm). **f)** The number of FG positive cells and corresponding FG intensity significantly decreases after the injury site in controls (red) (p=0.01102 and p=0.00278, respectively) as opposed to animals with scaffolds (blue) (p>0.05).

Conclusions

There has been significant hope in the treatment of SCI with the development of a multitude of natural and synthetic biomaterials[8,20,29,36,48–52]. Scaffolds composed of chitosan, collagen, hyaluronic acid, silk, methacrylate-derived poly-(2-hydroxyethyl) methacrylate and polyethylene glycol (PEG) have all demonstrated promising potential for SCI repair. Recently, researchers were able to create complex CNS structures in 3D printed PEG scaffolds[9]. This innovative approach led to the creation of scaffolds with microscale channels that mimicked the underlying architecture of the spinal cord in a rat model[9]. However, only once loaded with NPCs did these scaffolds result in animals achieving a BBB score of 6.6±0.5 after a complete transection injury. Consistent with our study, the channels in our scaffolds aided the sequestration of astrogliosis allowing for axonal projection[7]. Several previous studies have also demonstrated significantly increased BBB scores but only after scaffolds were loaded with NPCs and complementary agents to aid in neuroregeneration[9,31,32,52–55]. A common characteristic of these studies is that NPCs and other therapeutic approaches are required to stimulate any significant motor function recovery. In contrast, we observed an improvement in motor function similar to previous studies, without the necessity of loading scaffolds with therapeutic stem cells or other agents. Furthermore, to our knowledge only a small minority of studies have demonstrated that a non-degradable stable scaffold can lead to a consistent improvement in motor function over the course of six months in a rat model[30,56]. In contrast to many scaffold materials, we have shown that naturally derived plant cellulose scaffolds are biocompatible and become highly vascularized after implantation[12,13]. The low FBR and presence of significant vascularization in our scaffold aided both tissue infiltration/regeneration and also functional recovery without the need for therapeutic factors.

Biodegradability is often thought to be a necessary for implantable biomaterials[21]. However, natural biomaterials such as chitosan have shown some success in SCI while being non-degradable[48]. Plant-derived cellulose scaffolds are non-resorbable; however, they are highly biocompatible after implantation, structurally stable, and support tissue integration[12,13]. The scaffolds maintained their physical dimensions even after 6 months of implantation due to the lack of degradation. The scaffolds utilized here also do not display signs of chronic FBR and 86% of VBs become vascularized. Taken together, these results decrease the likelihood of the scaffolds being detrimental to motor recovery or require surgical removal. Host cells were able to infiltrate and pass through the full length of the VBs. Interestingly, scar tissue appeared to be sequestered in the largest of the VBs and we speculate that this phenomenon may be beneficial for the observed recovery. Finally, the FG results demonstrated that plant-derived scaffolds support axons from the stumps which are then able to form reconnections across the injury site.

The primary objective of this study was to establish that the microarchitectures found in plant-derived scaffolds can be exploited to repair neuronal tissues in SCI and offer a potential platform for future discovery and innovation. These exciting results demonstrate that such scaffolds are effective in supporting the regeneration of functional neural tissues in the most extreme model of traumatic SCI. In future work, we will explore the impact of loading scaffolds with NPCs as we expect a synergistic effect on improving regeneration and motor skill recovery. Acellular lignocellulosic scaffolds can be seeded with a vast array of cell types, as well as functionalized to include extra-cellular matrix proteins or neural growth factors through hydrogel loading and/or surface functionalization[24,57–60]. The emergence of plant-derived scaffolds for tissue engineering has opened up many new possibilities to regenerate target tissues of interest including soft tissues, muscle, and bone by exploiting plant microarchitectures[11–13,35,36,61,62]. The

14

results presented here demonstrate that such approaches can be exploited to aid in the regeneration of traumatic SCI, an incredibly complex injury model. The results point to exciting potential patient-treatment strategies in which plant-derived scaffolds might be deployed in combination with other therapeutics.

Methods

Biomaterial Production

This protocol is based on our previously published works[9–11]. Asparagus (*Asparagus officinalis)* was purchased from local supermarkets. The asparagus was stored at 4°C in the dark for a maximum of one week and kept hydrated. In order to prepare the scaffolds, the asparagus stalks (with a diameter 14–17 mm) were washed and the end of the stalks were cut to remove any dried tissue. The scaffolds were cut at different lengths using a #820 microtome (American Optical Company). The thickness of the asparagus scaffold was adjusted with the z-position block. The desired length of asparagus was cut with microtome blades (Westin Instruments Boston) in a quick motion to create two perpendicular surfaces with a precise length ranging from 0.2 mm – 1.6 cm. The resulting sections were then measured with a Vernier caliper. A 4 mm biopsy punch was used to cut out cylindrical sections close to the edges of the tissue to maximize the number of VBs. Effort was made to avoid the central fibrous tissues common in all angiosperm plants. Asparagus samples were placed in sterilized 2.5ml microcentrifuge tubes and 2ml of 0.1% sodium dodecyl sulphate (SDS) (Sigma-Aldrich) solution was added to each tube. Samples were shaken for 48 hours at 180 RPM at room temperature. The resulting cellulose scaffolds were then transferred into new sterile microcentrifuge tubes, washed and incubated for 12 hours in phosphate buffered saline (PBS) (Sigma-Aldrich). Following the PBS washing steps the

asparagus were then incubated in 100 mM CaCl$_2$ for 24 hours at room temperature to facilitate the removal of any of the remaining SDS. The samples were washed 3 times with dH$_2$O and then sterilized in 70% ethanol overnight. Finally, they were then washed 12 times with sterile saline solution and stored in saline. At this point, the samples were immediately used or stored at 4°C for no more than 24 hours.

Young's Modulus Testing

Scaffolds were loaded onto a CellScale UniVert (CellScale) compression platform. The Young's modulus was measured by compressing the material to a maximum 10% strain, at a compression speed of 50 μm/s. The force-indentation curves were converted to stress-strain curves and fitted in Origin 8.5. The Young's modulus was extracted from the elastic region of the curves.

Animal Care and Surgical Procedures

Female Sprague Dawley rats ranging in weight from 250-300 grams were purchased from Charles River. The rats were anesthetized with isoflurane USP-PPC (Pharmaceutical partners of Canada) and injected subcutaneously with normal saline (Baxter) and enrofloxacin (Baytril). Laminectomies were performed at the T8-T9 level to expose the spinal cord. The dura was incised with micro scissors to expose the spinal cord. A hook was passed ventrally to ensure the entire cord was within the bend of the hook. The spinal cord was carefully lifted with the hook and the entire cord was then cut with micro scissors. Both stumps of the spinal cord were carefully examined to confirm complete transection of spinal cord and spinal roots at that level. Surgifoam 1972 (Ethicon) was inserted into the gap between the two spinal cord stumps. After several minutes, when hemostatic control was established, the surgifoam was removed and the

16

resulting gap size was measured. Prior to the surgery, animals were randomly assigned as biomaterial or negative control. For animals assigned to the biomaterial group, a biomaterial scaffold was selected that best matched the gap distance of the stumps (range was typically 1to 3.5 mm). A volume of 0.2 mL Fibrin glue (Tisseel) was then applied to the dorsal surface to stabilize the biomaterial. Negative control animals had 0.2 mL fibrin glue placed between the two stumps. The muscle layers were then reapproximated with 3-0 Vicryl sutures (Johnson & Johnson) while the skin was closed with Michel clips (Fine Science Tools). Following the surgery, rats had their bladders expressed manually three times a day and were monitored for any symptoms of weight loss, dehydration, pain and urinary infections.

Functional studies

The locomotor function of the rats was assessed weekly based on the Basso Beattie Bresnahan (BBB) open-field assessment[42]. The rats were placed at the same time point in a 1-meter diameter arena once a week and was assessed by an independent blind observer while also being recorded from at least one view point for the entire duration of the cohort. Each of the five minutes videos of the rats was then scored by three blind observers and was averaged to get a weekly score. Any substantial spasticity and reflexes/twitches in any of the four joints were ignored and confirmed with repeated views of the videos.

Retrograde Tracer Surgery

Rats with biomaterial and controls were randomly selected at both time points (14 and 28 weeks) to undergo retrograde tracer. The rats were anesthetized and maintained with isoflurane USP-PPC (Pharmaceutical partners of Canada). A laminectomy was then performed at the T13 level

with a complete spinal cord transection performed as described in the previous spinal cord transections. In the spinal cord transection gap, a surgifoam (Ethicon,) soaked in 10 uL of 4% FluoroGold (Fluorochrome) in saline was placed onto the rostral end of the spinal cord stumps. Petroleum jelly (Sherwood Medical) was then added to stabilize the surgifoam into place and prevent nonspecific labelling before the muscles were then closed with 3-0 Vicryl. The skin was then closed with Michel suture clips (Fine Science Tools). The rats were allowed to recover and were monitored for 7 days to allow the FG travel.

Spinal Cord and Biomaterial Resection

For harvesting of the tissue, animals were sacrificed by intraperitoneal injection of 0.7–1.0 ml of sodium pentobarbital (65 mg/ml) and underwent intracardiac perfusion with 500 mL of normal saline and 0.5 U/mL heparin solution. The rats then perfused with 500 mL of 4% paraformaldehyde (Sigma-Aldrich,) in 0.1mM PBS(Sigma-Aldrich). The entire spinal cord and brain was then dissected out and further fixed overnight in 4% paraformaldehyde and 0.1mM phosphate buffer solution at 4°C. The tissue was then removed from the fixation solution and incubated in 30% sucrose (Sigma-Aldrich) 1% sodium azide (Sigma-Aldrich) in PBS for 24 hours at 4ºC. The biomaterial and the surrounding tissue were then frozen and mounted in Optimum Cutting Temperature compound (Stephens Scientific) with the remaining tissue fixed into paraffin. For tracer animals, the entire spinal cord and brain were frozen in individual blocks. Axial and sagittal sections of the tissue at 7–10 μm thick were then processed and mounted onto cold Superfrost Plus slides (Fisher Scientific) by the PALM Histology Core Facility at the University of Ottawa. Slides were stored in -80°C freezer until stained and mounted.

Histology and Immunohistochemistry

Frozen sections were stained with hematoxylin-eosin (H&E). Frozen sections were completely dried, rehydrated in 1X TBST buffer and blocked for 30 minutes with Rodent Block R (Biocare). Sections were then incubated overnight at 4°C with the following primary antibodies rabbit AB5804 GFAP (1:2000, Millipore) and mouse N0142 NF200 (1:3000, Sigma). The following day, the sections were washed with 1X TBST and then incubated with secondary antibodies: AB150077 Goat anti-rabbit 568 (Abcam) or AB175473 Goat anti-mouse 568 (Abcam) at 1:500 dilution for 2 hours in the dark at room temperature. Sections were washed with 1X TBST, incubated with 1ug/mL of DAPI (Thermo Scientific), washed, and then mounted in VectaShield Vibrance (Vector Laboratories) before adding a cover slip. The slides were kept in the dark at -20°C for a maximum of a week prior to imaging.

Microscopy

Micrographs of colorimetric stains were captured using Zeiss AxioScan Z1 slide Scanner (Zeiss) equipped with 10x objective and analyzed using ZenBlue (Zeiss, Canada) and ImageJ software. Phase microscopy was carried out on an A1R TiE inverted optical microscope (Nikon). Fluorescence imaging of tissue sections stained with NF200 and GFAP antibodies was carried out on a Nikon A1RsiMP Confocal Workstation with a 32-detector array for spectral imaging with 6 nm resolution detectors (Nikon). As lignocellulose can be auto fluorescent, spectral linear unmixing was achieved by imaging negative control scaffolds to obtain autofluorescence spectra. The spectral profile of the 568 antibody was then unmixed from any scaffold autofluorescence and the resulting unmixed z-stack was 3D deconvolved to create a projection. Although both

19

antibodies have the same 568nm wavelength fluorophore, for clarity NF200 data is presented as false-color green images to distinguish from false-color red GFAP data. FG slides samples were imaged with a Nikon Ni-U Ratiometric Fluorescence Microscope with a 340/380 filter set. All image processing was carried out with Nikon Elements software (Nikon).

Scanning Electron Microscopy

The structure of cellulose was studied using a SEM. Globally, scaffolds were fixed in an electron microscopy grade 4% PFA (Fisher Scientific) and dehydrated through successive gradients of ethanol (50%, 70%, 95% and 100%). The biomaterial was then dried with a critical point dryer (CPD) (SAMDRI-PVT-3D). Samples were then gold-coated at a current of 15mA for 3 minutes with a Hitachi E-1010 ion sputter device. SEM imaging was conducted at voltages ranging from 2.00–10.0 kV on a JSM-7500F Field Emission SEM (JEOL).

Statistics

All values reported here are the average ± standard error of the mean. Statistical analyses of the BBB scoring and scaffold volume were performed with one-way ANOVA by using SigmaStat 3.5 software (Dundas Software Ltd). A value of $p < 0.05$ was considered statistically significant.

Acknowledgments

Author Contributions

DJM oversaw the study and fabricated the scaffolds. DJM, CMC, RJH, MLL, IS, RKO, KLAW, AG participated in the surgeries and post-operative care for the animals. DJM, CMC, MLL, RJH, IS, RJO, KLAW, AG performed the BBB motor functioning testing. DJM, RJH, MLL, ECT performed the second transection and tracer surgeries. DJM performed the microscopy and tissue quantification. DJM, CMC, ECT, AEP participated in the histological analysis. AEP and ECT conceived, directed and managed the project. DJM, ECT and AEP reviewed the data and prepared the manuscript for publication.

Competing interests

DJM, CMC, RJH and AEP are inventors of patents regarding the creation and use of plant-derived cellulose biomaterials. DJM, CMC, RJH, MLL, IS and AEP were or are employees of

Spiderwort Inc. which is leading the clinical translation of these materials. All other authors declare no competing interests.

References

1. Theodore, N. *et al.* First human implantation of a bioresorbable polymer scaffold for acute traumatic spinal cord injury: A clinical pilot study for safety and feasibility. *Neurosurgery* **79**, E305–E312 (2016).

2. Yang, B. *et al.* Strategies and prospects of effective neural circuits reconstruction after spinal cord injury. *Curr. Stem Cell Res. Ther.* **15**, (2020).

3. Soares, S., von Boxberg, Y. & Nothias, F. Repair strategies for traumatic spinal cord injury, with special emphasis on novel biomaterial-based approaches. *Rev. Neurol. (Paris).* 1–9 (2020). doi:10.1016/j.neurol.2019.07.029

4. Ashammakhi, N. *et al.* Regenerative Therapies for Spinal Cord Injury. **25**, 471–491 (2019).

5. Zhou, P. *et al.* Cell Therapeutic Strategies for Spinal Cord Injury. *Adv. Wound Care* **8**, 585–605 (2019).

6. Moore, M. J. *et al.* Multiple-channel scaffolds to promote spinal cord axon regeneration. *Biomaterials* **27**, 419–429 (2006).

7. Stokols, S. & Tuszynski, M. H. Freeze-dried agarose scaffolds with uniaxial channels stimulate and guide linear axonal growth following spinal cord injury. *Biomaterials* **27**, 443–451 (2006).

8. Tsai, E. C., Dalton, P. D., Shoichet, M. S. & Tator, C. H. Matrix inclusion within synthetic hydrogel guidance channels improves specific supraspinal and local axonal regeneration

after complete spinal cord transection. *Biomaterials* **27**, 519–533 (2006).

9.   Koffler, J. *et al.* Biomimetic 3D-printed scaffolds for spinal cord injury repair. *Nat. Med.* (2019). doi:10.1038/s41591-018-0296-z

10.   Jiang, J. P. *et al.* Three-dimensional bioprinting collagen/silk fibroin scaffold combined with neural stem cells promotes nerve regeneration after spinal cord injury. *Neural Regen. Res.* **15**, 959–968 (2020).

11.   Modulevsky, D. J., Lefebvre, C., Haase, K., Al-Rekabi, Z. & Pelling, A. E. Apple Derived Cellulose Scaffolds for 3D Mammalian Cell Culture. *PLoS One* **9**, e97835 (2014).

12.   Modulevsky, D. J., Cuerrier, C. M. & Pelling, A. E. Biocompatibility of Subcutaneously Implanted Plant-Derived Cellulose Biomaterials. *PLoS One* **11**, 1–19 (2016).

13.   Hickey, R. J., Modulevsky, D. J., Cuerrier, C. M. & Pelling, A. E. Customizing the Shape and Microenvironment Biochemistry of Biocompatible Macroscopic Plant-Derived Cellulose Scaffolds. *ACS Biomater. Sci. Eng.* **4**, 3726–3736 (2018).

14.   Lucas, W. J. *et al.* The Plant Vascular System: Evolution, Development and Functions. *J. Integr. Plant Biol.* **55**, 294–388 (2013).

15.   Bessey, C. E. The Asparagus for Histological Study. *Bot. Gaz.* **6**, 294–295 (1881).

16.   Lenehan, B. *et al.* Demographics of acute admissions to a National Spinal Injuries Unit. *Eur. Spine J.* **18**, 938–942 (2009).

17.   McDonald, J. W., Becker, D. & Huettner, J. *Spinal Cord Injury*. *Handbook of Stem Cells* **2**, (Elsevier Inc., 2013).

18.   Partyka, P. P. *et al.* Harnessing neurovascular interaction to guide axon growth. *Sci. Rep.* **9**, 1–10 (2019).

19.   De Laporte, L., Lei Yan, A. & Shea, L. D. Local gene delivery from ECM-coated

poly(lactide-co-glycolide) multiple channel bridges after spinal cord injury. *Biomaterials* **30**, 2361–2368 (2009).

20. Tsintou, M., Dalamagkas, K., Seifalian, A. M. & Seifalian, M. A. Advances in regenerative therapies for spinal cord injury: a biomaterials approach. *Neural Regen. Res.* **10**, 726–742 (2015).

21. Straley, K. S. *et al.* Biomaterial Design Strategies for the Treatment of Spinal Cord Injuries. *J. Neurotrauma* **27**, 1–19 (2010).

22. Haggerty, A. E. & Oudega, M. Biomaterials for spinal cord repair. *Neurosci. Bull.* **29**, 445–459 (2013).

23. Liu, S., Schackel, T., Weidner, N. & Puttagunta, R. Biomaterial-Supported Cell Transplantation Treatments for Spinal Cord Injury: Challenges and Perspectives. *Front. Cell. Neurosci.* **11**, 430 (2018).

24. Mothe, A. J., Tam, R. Y., Zahir, T., Tator, C. H. & Shoichet, M. S. Repair of the injured spinal cord by transplantation of neural stem cells in a hyaluronan-based hydrogel. *Biomaterials* **34**, 3775–3783 (2013).

25. Shrestha, B. *et al.* Repair of injured spinal cord using biomaterial scaffolds and stem cells. *Stem Cell Res. Ther.* (2014). doi:10.1186/scrt480

26. Slotkin, J. R. *et al.* Biodegradable scaffolds promote tissue remodeling and functional improvement in non-human primates with acute spinal cord injury. *Biomaterials* **123**, 63–76 (2017).

27. Novikova, L. N., Novikov, L. N. & Kellerth, J. Biopolymers and biodegradable smart implants for tissue regeneration after spinal cord injury. 711–715 (2003). doi:10.1097/01.wco.0000102620.38669.3e

28. Warburton, A., Girdler, S. J., Mikhail, C. M., Ahn, A. & Cho, S. K. Biomaterials in Spinal Implants: A Review. *Neurospine* 1–10 (2019). doi:10.14245/ns.1938296.148

29. Boni, R., Ali, A., Shavandi, A. & Clarkson, A. N. Current and novel polymeric biomaterials for neural tissue engineering. *J. Biomed. Sci.* **25**, 1–21 (2018).

30. Ruzicka, J. *et al.* The Effect of iPS-Derived Neural Progenitors Seeded on Laminin-Coated pHEMA-MOETACl Hydrogel with Dual Porosity in a Rat Model of Chronic Spinal Cord Injury. *Cell Transplant.* **28**, 400–412 (2019).

31. Li, X. *et al.* Scaffold-facilitated locomotor improvement post complete spinal cord injury: Motor axon regeneration versus endogenous neuronal relay formation. *Biomaterials* **197**, 20–31 (2019).

32. S, H. *et al.* Human Placenta-Derived Mesenchymal Stem Cells Loaded on Linear Ordered Collagen Scaffold Improves Functional Recovery After Completely Transected Spinal Cord Injury in Canine. *Sci. China. Life Sci.* **61**, (2018).

33. W, Y. *et al.* Taxol-modified Collagen Scaffold Implantation Promotes Functional Recovery After Long-Distance Spinal Cord Complete Transection in Canines. *Biomater. Sci.* **6**, (2018).

34. Chen, X. *et al.* Functional Multichannel Poly(Propylene Fumarate)-Collagen Scaffold with Collagen-Binding Neurotrophic Factor 3 Promotes Neural Regeneration After Transected Spinal Cord Injury. *Adv. Healthc. Mater.* **7**, 1800315 (2018).

35. Gershlak, J. R. *et al.* Crossing kingdoms: Using decellularized plants as perfusable tissue engineering scaffolds. *Biomaterials* **125**, 13–22 (2017).

36. Fontana, G. *et al.* Biofunctionalized Plants as Diverse Biomaterials for Human Cell Culture. *Adv. Healthc. Mater.* **6**, 1601225 (2017).

37. Zhang, J. *et al.* Perfusion-decellularized skeletal muscle as a three-dimensional scaffold with a vascular network template. *Biomaterials* **89**, 114–126 (2016).

38. Park, M. *et al.* Control over Neurite Directionality and Neurite Elongation on Anisotropic Micropillar Arrays. *Small* **12**, 1148–1152 (2016).

39. Silva, N. A., Sousa, N. & Reis, R. L. Progress in Neurobiology From basics to clinical : A comprehensive review on spinal cord injury. **114**, 25–57 (2014).

40. Norenberg, M. D., Smith, J. O. N. & Marcillo, A. The Pathology of Human Spinal Cord Injury : Defining the Problems. **21**, 429–440 (2004).

41. Cripps, R. A. *et al.* A global map for traumatic spinal cord injury epidemiology: Towards a living data repository for injury prevention. *Spinal Cord* **49**, 493–501 (2011).

42. Basso, D. M., Beattie, M. S. & Bresnahan, J. C. A Sensitive and Reliable Locomotor Rating Scale for Open Field Testing in Rats. *J. Neurotrauma* **12**, 1–21 (1995).

43. Anderson, M. A. *et al.* Astrocyte scar formation aids CNS axon regeneration. *Nature* **532**, 195–200 (2016).

44. Hackett, A. R. & Lee, J. K. Understanding the NG2 glial scar after spinal cord injury. *Front. Neurol.* **7**, 1–10 (2016).

45. Yang, T., Dai, Y. J., Chen, G. & Cui, S. Sen. Dissecting the Dual Role of the Glial Scar and Scar-Forming Astrocytes in Spinal Cord Injury. *Front. Cell. Neurosci.* **14**, (2020).

46. Hoffman-Kim, D., Mitchel, J. A. & Bellamkonda, R. V. Topography, cell response, and nerve regeneration. *Annu. Rev. Biomed. Eng.* **12**, 203–31 (2010).

47. Tsai, E. C., van Bendegem, R. L., Hwang, S. W. & Tator, C. H. A novel method for simultaneous anterograde and retrograde labeling of spinal cord motor tracts in the same animal. *J. Histochem. Cytochem.* **49**, 1111–1122 (2001).

26

48.   Kim, H., Tator, C. H. & Shoichet, M. S. Chitosan implants in the rat spinal cord: Biocompatibility and biodegradation. *J. Biomed. Mater. Res. - Part A* **97 A**, 395–404 (2011).

49.   Pakulska, M. M., Tator, C. H. & Shoichet, M. S. Local delivery of chondroitinase ABC with or without stromal cell-derived factor 1α promotes functional repair in the injured rat spinal cord. *Biomaterials* **134**, 13–21 (2017).

50.   Pravincumar, P., Bader, D. L. & Knight, M. M. Viscoelastic cell mechanics and actin remodelling are dependent on the rate of applied pressure. *PLoS One* **7**, e43938 (2012).

51.   Ziemba, A. M. & Gilbert, R. J. Biomaterials for local, controlled drug delivery to the injured spinal cord. *Front. Pharmacol.* **8**, 1–20 (2017).

52.   Badhiwala, J. H., Ahuja, C. S. & Fehlings, M. G. Time is spine: A review of translational advances in spinal cord injury. *J. Neurosurg. Spine* **30**, 1–18 (2019).

53.   Li, X. *et al.* A collagen microchannel scaffold carrying paclitaxel-liposomes induces neuronal differentiation of neural stem cells through Wnt/β-catenin signaling for spinal cord injury repair. *Biomaterials* **183**, 114–127 (2018).

54.   Ganz, J. *et al.* Implantation of 3D Constructs Embedded with Oral Mucosa-Derived Cells Induces Functional Recovery in Rats with Complete Spinal Cord Transection. *Front. Neurosci.* **11**, 589 (2017).

55.   B, X. *et al.* A Dual Functional Scaffold Tethered With EGFR Antibody Promotes Neural Stem Cell Retention and Neuronal Differentiation for Spinal Cord Injury Repair. *Adv. Healthc. Mater.* **6**, (2017).

56.   Tamosaityte, S. *et al.* Biochemical Monitoring of Spinal Cord Injury by FT-IR Spectroscopy—Effects of Therapeutic Alginate Implant in Rat Models. *PLoS One* **10**,

e0142660 (2015).

57.   Pakulska, M. M., Vulic, K. & Shoichet, M. S. Affinity-based release of chondroitinase ABC from a modified methylcellulose hydrogel. *J. Control. Release* **171**, 11–16 (2013).

58.   Gupta, D., Tator, C. H. & Shoichet, M. S. Fast-gelling injectable blend of hyaluronan and methylcellulose for intrathecal, localized delivery to the injured spinal cord. *Biomaterials* **27**, 2370–2379 (2006).

59.   Pértile, R. A. N., Moreira, S., Gil, R. M., Correia, A. & Guãrdao, L. Bacterial Cellulose : Long-Term Biocompatibility Studies. *J. Biomater. Sci. Polym. Ed.* **23**, 1339–1354 (2012).

60.   Klemm, D., Heublein, B., Fink, H. P. & Bohn, A. Cellulose: fascinating biopolymer and sustainable raw material. *Angew. Chem. Int. Ed. Engl.* **44**, 3358–93 (2005).

61.   Wang, Y., Dominko, T. & Weathers, P. J. Using decellularized grafted leaves as tissue engineering scaffolds for mammalian cells. *Vitr. Cell. Dev. Biol. - Plant 2020* 1–10 (2020). doi:10.1007/S11627-020-10077-W

62.   Lee, J., Jung, H., Park, N., Park, S. H. & Ju, J. H. Induced Osteogenesis in Plants Decellularized Scaffolds. *Sci. Rep.* **9**, 1–10 (2019).